

Multiple topological electronic phases in superconductor MoC

Angus Huang,^{1,2} Adam D. Smith,² Madison Schwinn,² Qiangsheng Lu,² Tay-Rong Chang,³ Weiwei Xie,⁴ Horng-Tay Jeng,^{1,5,6,*} and Guang Bian^{2,†}

¹*Department of Physics, National Tsing Hua University, Hsinchu 30013, Taiwan*

²*Department of Physics and Astronomy, University of Missouri, Columbia, Missouri 65211, USA*

³*Department of Physics, National Cheng Kung University, Tainan 701, Taiwan*

⁴*Department of Chemistry, Louisiana State University, Baton Rouge, Louisiana 70803, USA*

⁵*Institute of Physics, Academia Sinica, Taipei 11529, Taiwan*

⁶*Physics Division, National Center for Theoretical Sciences, Hsinchu 30013, Taiwan*



(Received 16 September 2017; revised manuscript received 7 March 2018; published 22 May 2018)

The search for a superconductor with non- s -wave pairing is important not only for understanding unconventional mechanisms of superconductivity but also for finding new types of quasiparticles such as Majorana bound states. Materials with both topological band structure and superconductivity are promising candidates as $p + ip$ superconducting states can be generated through pairing the spin-polarized topological surface states. In this work, the electronic and phonon properties of the superconductor molybdenum carbide (MoC) are studied with first-principles methods. Our calculations show that nontrivial band topology and s -wave Bardeen–Cooper–Schrieffer superconductivity coexist in two structural phases of MoC, namely the cubic α and hexagonal γ phases. The α phase is a strong topological insulator and the γ phase is a topological nodal-line semimetal with drumhead surface states. In addition, hole doping can stabilize the crystal structure of the α phase and elevate the transition temperature in the γ phase. Therefore, MoC in different structural forms can be a practical material platform for studying topological superconductivity.

DOI: [10.1103/PhysRevMaterials.2.054205](https://doi.org/10.1103/PhysRevMaterials.2.054205)

I. INTRODUCTION

The search for topological superconducting materials has sparked tremendous research interest in the solid-state physics community, because topological superconductors host Majorana fermion quasiparticles on their boundaries. The Majorana quasiparticles have been proposed to be the cornerstone for fault-tolerant topological computations [1,2]. One practical route to realizing topological superconductivity is simultaneously combining superconductivity and nontrivial electronic band structure in a single compound. The topological electronic materials, including topological insulators and topological semimetals, possess symmetry-protected surface states [3–8], and those surface states usually show nontrivial spin texture in accordance with the nontrivial band topology. For example, the spin and momentum of Dirac surface states in a topological insulator are locked in a helical fashion. When the topological surface electrons form Cooper pairs in a superconducting state, then an effective time-reversal symmetric $p + ip$ pairing naturally emerges as a consequence of the topological constraint [9–11]. This topological superconducting phase can host Majorana fermions [12,13] or supersymmetric particles [14] which have never been experimentally observed in elementary particles. Therefore, it is of fundamental research interest to identify superconductors with nontrivial band topology. Several such materials have been predicted and synthesized in the form of topological

insulator/superconductor heterostructures [11,14,15] and superconducting topological insulators such as Cu-doped Bi_2Se_3 , PbTaSe_2 , and BiPd [16–24]. Though there has been experimental evidence for Majorana fermions in some of these materials [15], two adverse factors obscure a clear picture of Majorana modes: one is the complex configuration of the heterostructures and the other is low superconducting transition temperature T_C , usually below 4 K. Therefore, there is a pressing need for the identification of new superconducting compounds with simple composition, high transition temperature, and nontrivial electronic band topology.

In this paper, we use first-principles methods to study two structural phases of molybdenum monocarbide (MoC), namely α -MoC and γ -MoC. The superconductive α -MoC phase forms in the rock-salt crystal structure with C deficiency and has a $T_C \simeq 14$ K [25–27]. γ -MoC, on the other hand, takes a noncentrosymmetric hexagonal structure and is not superconducting in its pristine form. We show that α -MoC possesses a nonzero \mathbb{Z}_2 topological invariant and Dirac surface states. γ -MoC, on the other hand, is a topological nodal-line semimetal with drumhead surface states. Moreover, we simulate under the virtual crystal approximation [28,29], and predict that the γ phase of MoC gains superconductivity by hole doping and T_C can be tuned to be higher than 9 K. Therefore, both phases of MoC can be material candidates for studying topological superconductors and their exciting fundamental physics.

II. LATTICE STRUCTURE AND BULK BANDS

The α phase of MoC has a rock-salt crystal structure with space group 225 ($Fm\bar{3}m$) and the experimental lattice constant

*jeng@phys.nthu.edu.tw

†biang@missouri.edu

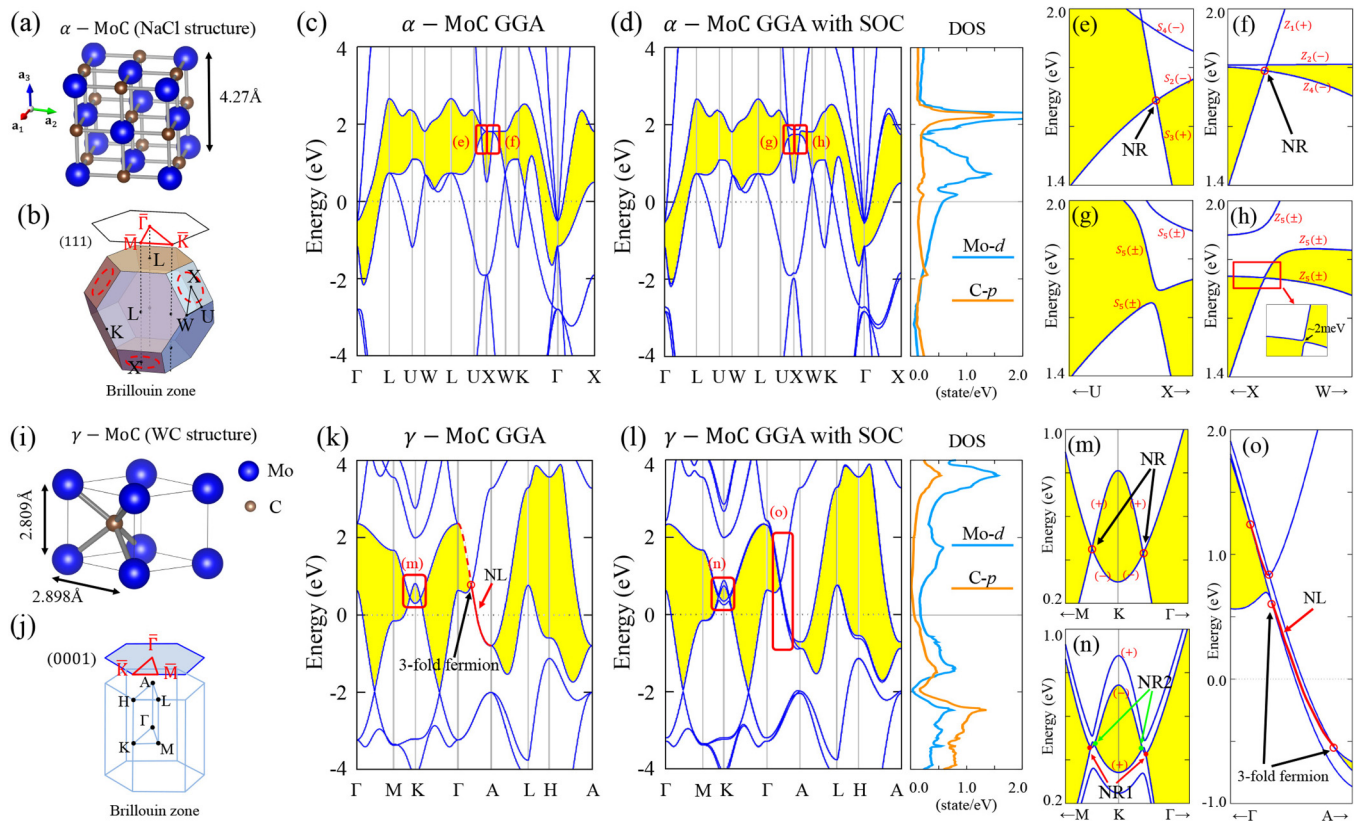


FIG. 1. (a) The lattice structure of α -MoC. The Mo and C atoms are represented by blue and brown balls, respectively. (b) The first Brillouin zone and (111)-surface Brillouin zone of α -MoC. [(c) and (d)] The bulk band structure and density of states (DOS) of α -MoC without and with SOC, respectively. A continuous bulk gap is highlighted in yellow color. [(e)–(h)] The zoom-in band crossings marked in (a) and (b). The symmetry (space group representation) are labeled and the mirror eigenvalue in the XUW mirror plane is given by + or – sign. In (e) and (f), the nodal ring (NR) surrounding X are marked with red circles. The band crossing is protected by the mirror symmetry. [(i)–(l)] Same as in (a)–(d), but for γ -MoC. In (j), the (001) surface Brillouin zone is plotted. [(m) and (n)] The zoom-in nodal-ring band structure surrounding the K point marked in (k) and (l), respectively. The mirror eigenvalue in the ΓKM plane is labeled by + or – sign. (o) The zoom-in band structure of γ -MoC between ΓA as marked in (l). The nodal lines (NL, red lines) connect threefold degenerate bulk nodes (red circles).

is 4.27 Å [30]; see Fig. 1(a). The structure is centrosymmetric, and both the Mo atom and the C atom in the unit cell can be regarded as a space inversion center. The first Brillouin zone, a truncated octahedron (same as FCC), is shown in Fig. 1(b) with the high-symmetry points labeled. The bulk band calculation without the inclusion of spin-orbit coupling (SOC) shows that there is a band gap between the valence and conduction bands [highlighted in yellow color in Fig. 1(c)] and the gap closes at two points that lie in $X-W$ and $U-X$ as marked in Fig. 1(c). To check these bulk nodal points, we calculated the symmetry properties of the two bands. The space group representation is labeled in the zoomed-in band structure in Figs. 1(e) and 1(f). We find that the two bands that form the bulk band nodes have opposite mirror eigenvalues with respect to the mirror plane WXU . Therefore, the intersection of the two bands is protected by the mirror symmetry and the crossing points form a one-dimensional (1D) loop surrounding the X point in the WXU plane as schematically drawn in Fig. 1(b). This indicates that α -MoC is a nodal line semimetal in the absence of SOC [9,31–34].

Generally, the nodal-line band structure is unstable in a centrosymmetric system once SOC is included [9]. With space inversion and time-reversal symmetries, every band is doubly

degenerate with respect to spin (we note that with the inclusion of SOC, the spin is not a good quantum number, because SOC does not conserve spin degree of freedom. It is more accurate to use pseudospin to describe the spin degree of freedom in spin-orbit coupled materials), and the two spin-degenerate subbands carry opposite mirror eigenvalues if the band lies in a mirror plane. So when two spin-degenerate bands cross, the spin subbands with the same mirror eigenvalue repel each other and form a SOC-induced band gap. This is exactly what we find in the band structure of α -MoC with SOC taken into consideration; see Figs. 1(d), 1(g) and 1(h). The bulk nodal line is gapped when SOC is turned on in the calculation. The overall band dispersion changes very little owing to the weak atomic SOC of molybdenum and carbon atoms. The fact that a band crossing is gapped by SOC strongly implies that this phase possesses a nontrivial band topology. We will show this later in the discussion on the \mathbb{Z}_2 topological invariant and the topological surface states of α -MoC.

The other structural phase we studied is γ -MoC which has a noncentrosymmetric hexagonal structure (space group 187, $P\bar{6}m2$) like tungsten monocarbide (WC); see Fig. 1(i). The lattice constants are $a = 2.898$ Å and $c = 2.809$ Å [35]. The WC structure is composed of hexagonal atomic layers which

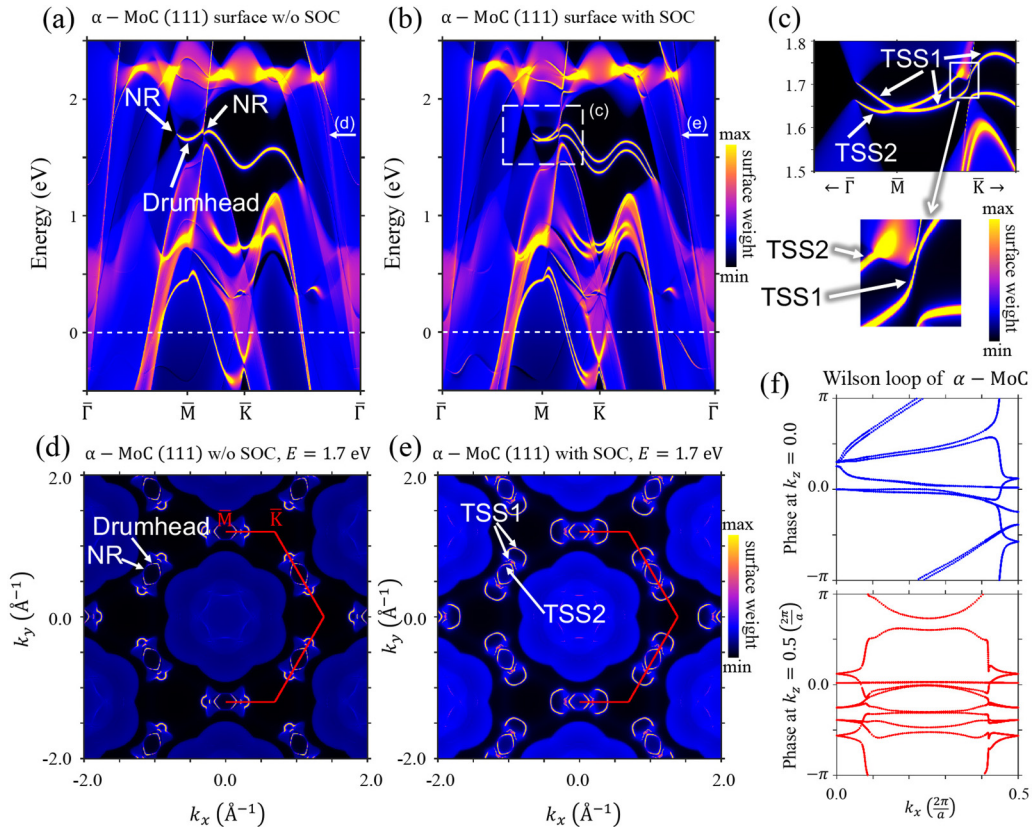


FIG. 2. [(a) and (b)] Band spectrum of semi-infinite α -MoC without and with the inclusion of SOC, respectively. The bands are colored according to the surface weight of each state. (c) The zoom-in topological surface band structure marked in (b). [(d) and (e)] The isoenergy band contour at $E = 1.7$ eV without and with SOC, respectively. The energy value is marked by white arrows in (a) and (b). (f) The calculated Wilson loop showing a nonzero \mathbb{Z}_2 topological invariant.

stack along the (001) direction. The Mo layer is sandwiched between two C layers in an ABA fashion, and this trilayer structure forms the unit cell of γ -MoC. The first Brillouin zone and the high-symmetry points of WC structure are depicted in Fig. 1(j). The calculated bulk bands with and without SOC are shown in Figs. 1(k) and 1(l). The bulk band gap is highlighted in yellow. In the case without SOC, there are two gapless features near the Fermi level. One is a bulk nodal ring (loop-shaped nodal line) surrounding the K point. Similarly to the case of α -MoC without SOC, the nodal ring is protected by the mirror symmetry with respect to the ΓMK plane, which can be seen from mirror parity eigenvalues labeled in Fig. 1(m). The other feature is a band crossing of a doubly degenerate band [the red solid and dashed lines in Fig. 1(k)] and a singly degenerate band along the Γ - A direction. The doubly degenerate band is a two-component representation of the “little” space group in the Γ - A direction. Thus, the degeneracy of the crossing point marked by a red circle in Fig. 1(k) is three, which was referred to as “class α threefold fermion” in the literature [36]. The band plotted with a red solid line can be regarded as a bulk nodal line in the form of an open curve. When SOC is included, each band splits into two spinful subbands due to the lack of space inversion symmetry while the double band transforms into two spinful double bands as shown in Figs. 1(l), 1(n), and 1(o). The nodal ring now becomes two copies of spinful nodal rings which remain gapless due to the protection of mirror reflection symmetry [33,34,37]; see Fig. 1(n). Along Γ - A , four threefold

fermion nodes form due to the band splitting. They are connected by two doubly degenerate nodal lines as demonstrated in Fig. 1(o) [36,37]. Here we note the difference between the Γ - A nodal line and the nodal ring surrounding the K point. The nodal lines connecting two threefold fermion nodes are protected by the threefold rotational symmetry along Γ - A while the nodal ring is protected by the mirror reflection symmetry.

III. TOPOLOGICAL INVARIANT AND SURFACE BAND STRUCTURE

The topological invariant and surface bands of the two phases of MoC are calculated and the results show that both phases are topologically nontrivial in their bulk and surface band structure; see Figs. 2 and 3. The nodal ring of α -MoC is gapped by SOC, resulting in a continuous band gap that traverses the whole Brillouin zone. The crystal lattice of α -MoC has space inversion symmetry, so the \mathbb{Z}_2 topological invariant can be determined by the parity eigenvalues of all valence bands at the eight time-reversal invariant momentum (TRIM) points which are $\Gamma(1)$, $X(3)$, $L(4)$, for α -MoC. According to our calculations, the product of parity eigenvalues is -1 , 1 , and 1 for Γ , X , and L , respectively. Therefore, the \mathbb{Z}_2 topological invariant is $\nu_{\mathbb{Z}_2} = \prod_{i \in \text{TRIM}} P_i = -1$, indicating α -MoC is a topological metal with nontrivial band topology [38]. We also calculated the \mathbb{Z}_2 topological invariant by the

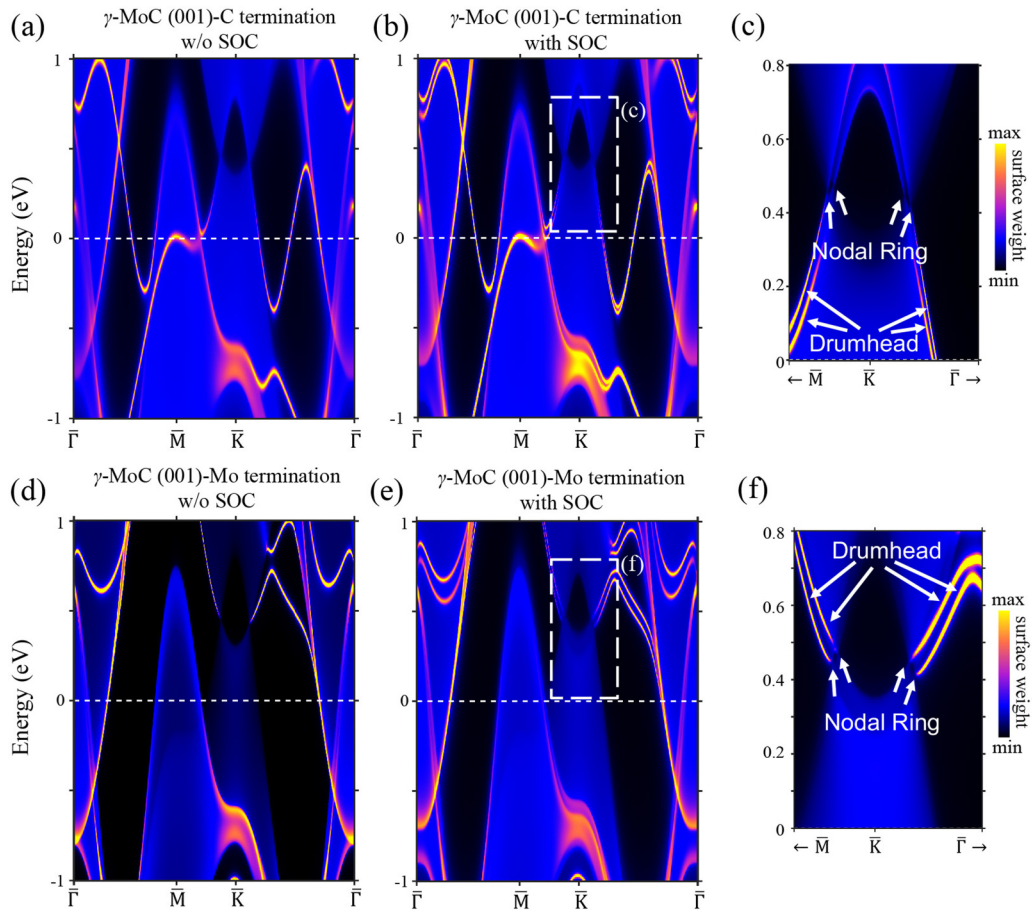


FIG. 3. [(a) and (b)] Band spectrum of semi-infinite γ -MoC without and with the inclusion of SOC, respectively. The bands are colored according to the surface weight of each state. The surface is terminated in the (001) direction with a C top layer. (c) The zoom-in nodal-line band structure marked in (b). [(d)–(f)] Same as in (a)–(c) but for a Mo-terminated (001) surface.

Wilson loop method [39]; see Fig. 2(f). The Wilson band is an open curve traversing the entire Brillouin zone in the time reversal invariant plane $k_z = 0$ and a closed loop in another time-reversal invariant plane $k_z = 0.5\pi$. The result indicates that the \mathbb{Z}_2 invariant equals 1, which is consistent with the result from our parity calculations.

The surface states of α -MoC are calculated in a semi-infinite slab geometry with (111) surface termination. The bulk and surface bands of α -MoC (111) with and without SOC are plotted in Figs. 2(a) and 2(b). In the case without SOC, the bulk nodal ring (NR) surrounds the \bar{M} point which corresponds to the projection of X to the (111) surface Brillouin zone. The 2D drumhead surface band connects to the bulk band nodes inside the ring as marked in Fig. 2(a). There is an extra surface band lying outside the nodal ring along \bar{M} - \bar{K} . When SOC is included, the bulk nodal ring is gapped and the material becomes a topological insulator (strictly speaking, it is a topological metal, because there are irrelevant bulk bands around the Fermi level). The drumhead surface band transforms into topological Dirac surface states. We note that the surface band outside the nodal ring splits into two subbands, one of which is connected to the lower branch of the Dirac cone as shown in the zoomed-in bands in Fig. 2(c). With this connection to the outer surface band, the Dirac cone extends to the valence bulk band along \bar{M} - \bar{K} - $\bar{\Gamma}$ and form a gapless

dispersion connecting the conduction and valence bulk bands as required by the band topology. The dispersion of the surface bands in the presence of SOC again proves that α -MoC is a topological metal with nontrivial band topology. The 2D isoenergy contours are plotted in Figs. 2(d) and 2(e) for the cases without and with SOC, respectively. The energy is set to 1.7 eV, which is the energy value of the bulk node in the Γ - M direction. The nodal ring, drumhead surface states and topological Dirac surface states can be seen in the contour. Interestingly, the surface state outside the nodal ring form a surface arc with both its ends connected to the bulk electron pocket as shown in Fig. 2(d).

There is no absolute band gap in γ -MoC, so the \mathbb{Z}_2 topological invariant cannot be defined in this phase. Instead, we can calculate the winding number associated with the nodal ring around the K point. The winding number has been shown to be equal to a mirror Chern number n^+ which is defined as the difference between the number of valence bands with a $+1$ mirror eigenvalue inside and outside the nodal ring [33]. $n^+ = -1$ for the nodal ring according to the result in Fig. 1(m). In the presence of SOC [Fig. 1(n)], $n^+ = \pm 1$ for inner and outer nodal rings, respectively. The winding number is a topological invariant and it determines the number of drumhead surface bands emanating from the nodal ring. To show this, we calculated the surface bands of γ -MoC in a

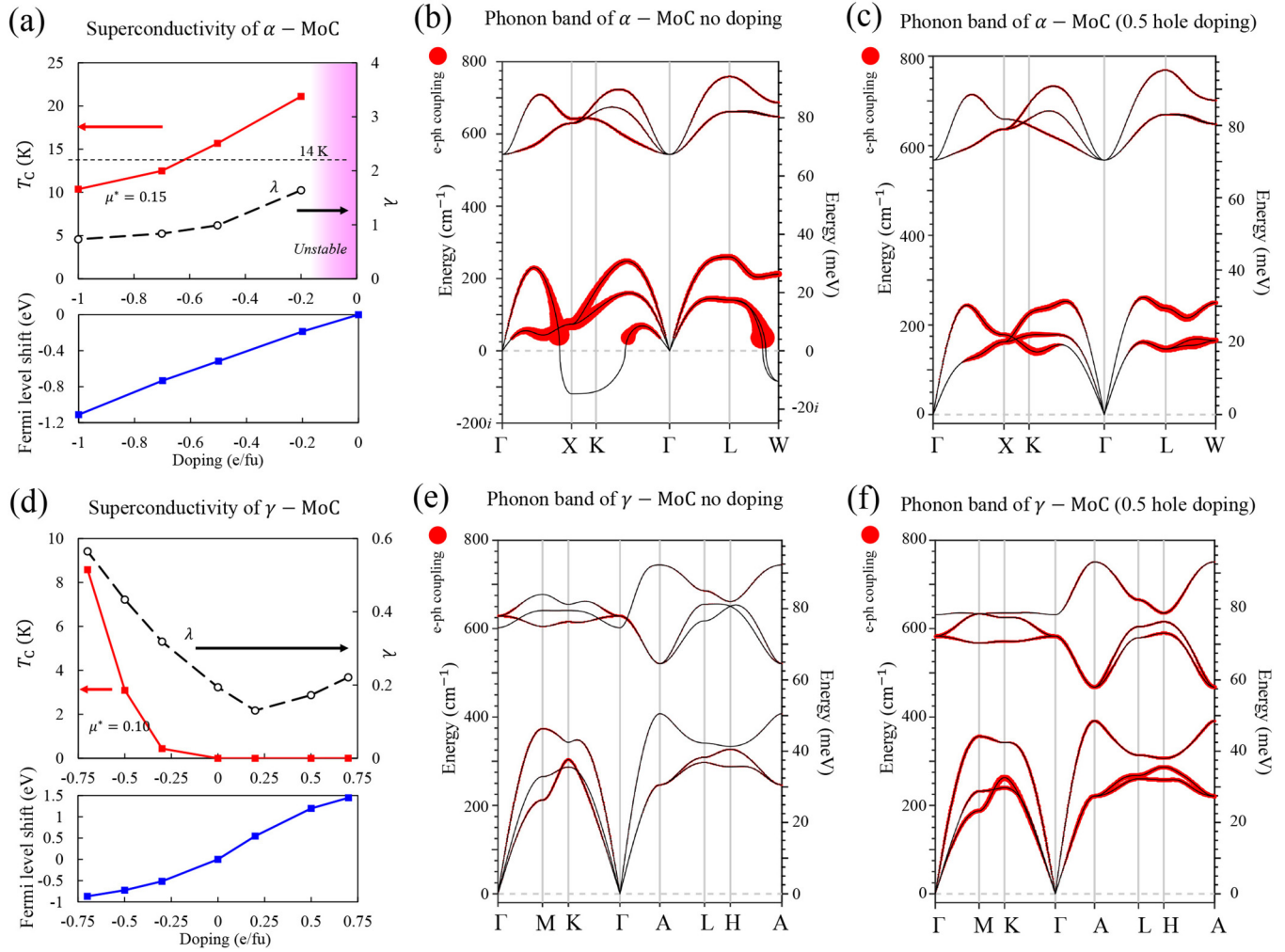


FIG. 4. Calculated phonon dispersion and superconducting transition temperature of MoC in two phases. (a) The transition temperature (red line) and electron-phonon coupling strength λ (black dashed line) of α -MoC as a function of doping concentration (negative values correspond to hole doping). The energy shift of Fermi level as a function of doping is plotted in the lower subfigure. [(b) and (c)] The phonon bands of α -MoC without doping and with -0.5 e/fu doping, respectively. The thickness of red line indicates the strength of electron-phonon coupling. [(d)–(f)] Same as in (a)–(c) but for γ -MoC.

semi-infinite slab geometry with the (001) surface. There are two possible terminations: One is with a C top layer and the other with a Mo top layer. In both cases, we found a single nodal ring surrounding the \bar{K} in the bulk band and a drumhead surface band which disperses outwards from the ring in the absence of SOC; see Fig. 3. When SOC is considered, the nodal ring splits into two copies of Weyl nodal rings and each Weyl nodal ring is connected to a spinful drumhead surface band [33]. The drumhead bands in the cases of C and Mo terminations have opposite signs in their slope outside the ring, which can be attributed to the dramatically different atomic electronegativity of C and Mo surface layers.

IV. ELECTRON-PHONON COUPLING AND SUPERCONDUCTIVITY

To investigate the superconductivity and electron-phonon coupling (EPC) properties of the two phases of MoC, we performed a systematic density functional perturbation theory (DFPT) simulation (see Sec. VI for details). We found that

α -MoC is unstable in its pristine form and the phonon bands have imaginary frequencies, which is consistent with previous theoretical studies [40–42]. In experiments, the α phase of MoC has been synthesized but with C deficiency ($\text{MoC}_{1-\delta}$) [26,43]. The C deficiency effectively lowers the Fermi level since the total number of electrons per formula unit decreases [27]. To simulate the effect of C deficiency, we calculated the EPC and phonon properties with hole doping under the virtual crystal approximation [28]; see Fig. 4(a). We found that α -MoC is indeed unstable in its pristine form. The phonon bands have imaginary frequencies, consistent with previous theoretical studies. When the hole doping increases to be more than -0.2 electron per formula unit (-0.2 e/fu), the imaginary phonon band disappears [Fig. 4(c)] and the lattice is stabilized. This suggests that α -MoC with hole doping can be a stable superconducting phase, which is in accordance with the experimental results. We note that previous studies suggest that the Coulomb repulsion μ^* may increase in transition metal carbides and transition metal nitride [40,42]. This occurs in disordered structures because defects can enhance the electron-

electron Coulomb interaction [44]. In our simulations, we set $\mu^* = 0.15$, which is larger than the commonly adopted value of 0.1, to take into account the defect effect. The transition temperature is $T_C \simeq 21.1$ K at doping level -0.2 *e*/fu and decreases gradually with the increasing concentration of hole doping. $T_C = 15.7$ K for -0.5 *e*/fu hole doping, which is similar to the experimental value of 14.3 K [25]. Further increasing hole doping to -1.0 *e*/fu brings T_C down to 10.4 K. This is consistent with the experimental results from NbC ($T_C \simeq 11.1$ K) [25], since Nb has one less electron compared to Mo. The trend of T_C with varied doping agrees well with the experiment values obtained from MoC-NbC alloy [25].

In the case without doping, one of acoustic phonon bands of α -MoC becomes imaginary near the *X* point; see Fig. 4(b). The EPC strength (represented by the red line thickness) diverges as the phonon energy approaches zero along Γ -*X*. Both facts indicate that the crystal structure of α -MoC is unstable. Doping holes into the compound can remove the imaginary phonon modes and create soft acoustic modes around *X*. Those soft phonon modes couple strongly with electronic states and thus dominantly contribute to the effective EPC in the Bardeen–Cooper–Schrieffer theory; see Fig. 4(c). Therefore, the structural instability of α -MoC is responsible for the high transition temperature observed in this phase. The close relationship of superconductivity and structural instability has also been found in materials with charge density waves (CDW). Suppressing CDW may generate superconductivity in CDW materials, such as in Cu_xTaS_2 [45] and PbTaSe_2 [16]. As the hole doping concentration increases, the soft phonon modes become normal phonon modes. At the same time, the effective EPC becomes weaker and, consequently, the superconducting transition temperature T_C decreases as shown in Fig. 4(a).

Unlike α -MoC, the crystal structure of γ -MoC is stable in its pristine form but superconductivity has not been observed in γ -MoC. We calculated the transition temperature of γ -MoC with various doping concentrations and the result is plotted in Fig. 4(d). T_C is negligibly small with or without electron doping. Hole doping, on the other hand, can induce superconductivity in γ -MoC. Doping 0.3 holes per formula unit can lift T_C to 0.4 K, and T_C increases rapidly as the hole doping concentration further increases. For example, $T_C \simeq 8.6$ K at hole doping level -0.7 *e*/fu.

The phonon band and EPC of γ -MoC with different levels of hole doping are shown in Figs. 4(e) and 4(f). The phonon dispersion only changes slightly by increasing the doping level, but the EPC is remarkably enhanced for almost all phonon bands. The enhancement of EPC and superconductivity in γ -MoC by hole doping can be attributed to the increase in the electron density of states (DOS), especially when the Fermi level passes the Van Hove singularity of DOS at about 0.8 eV below the Fermi level at the *H* and *A* points. Thus we predict that hole-doped γ -MoC is a superconducting nodal-line semimetal with drumhead surface states.

V. CONCLUSION

In summary, we performed a systematic first-principles study of the two structural phases of MoC. α -MoC is a superconductor with a considerably high T_C of 14 K. The pristine rocksalt lattice of α -MoC is unstable according to

our phonon calculations. However, it can be stabilized by hole doping, which is in line with the fact that the chemically synthesized α -MoC carries carbon vacancies. The high transition temperature of α -MoC is connected with the suppression of structural instability. Moreover, α -MoC is a topological metal with a nonzero topological \mathbb{Z}_2 invariant. The Dirac surface band is located at 1.7 eV above the Fermi level. γ -MoC, on the other hand, is not superconducting in its pristine form. Hole doping can make the compound a superconductor. The transition temperature can be as high as 9 K if 0.75 hole is doped per unit cell. We also found that γ -MoC is a topological nodal-line semimetal with a pair of nodal rings surrounding the *K* point and drumhead surface states. We note that topological surface bands of α -MoC are located above the Fermi level, so the proposed $p + ip$ superconductivity can be achieved in α -MoC only when the Fermi level can be shifted to the energy region of the surface states by either electrical gating or chemical doping. The superconductivity should be preserved when the Fermi level is shifted in order to pair up topological surface electrons of α -MoC. The topological surface bands (drumhead) of γ -MoC (with C termination) lie around the Fermi level. Therefore, nontrivial superconducting pair can possibly occur in γ -MoC. Besides MoC, transition-metal monocarbides, XC ($X = \text{W}, \text{Ta}, \text{Nb}$) and transition metal mononitrides, XN ($X = \text{V}, \text{Nb}, \text{Ti}$) are all superconductors [46,47], and meanwhile they can host a large variety of band topology in their different structural forms. Therefore, these compounds provide an exciting family of candidate materials for studying the rich physics in topological superconductors and Majorana bound states.

VI. METHODS

The first-principles electronic structure simulations are based on the density functional theory (DFT) which is implemented in VASP packages [48–50]. The Perdew–Burke–Ernzerhof-type [51] generalized-gradient-approximation functionals and projector-augmented-wave-type pseudopotential [52,53] are used in the calculations. The lattice parameters are taken from experimental values. A $24 \times 24 \times 24$ *k* grid and an energy cutoff of 400 eV are used in the band structure calculations. The vasp2wannier90 interface [54] is used to construct the Wannier Hamiltonian of semi-infinite slabs. The surface band spectrum is obtained from the Green function of semi-infinite slabs [55]. The topological \mathbb{Z}_2 invariant is calculated from the phase of Wannier centers [56].

The calculations of electron-phonon coupling and superconductivity are based on the density functional perturbation theory (DFPT). Quantum Espresso packages are employed with norm-conserving pseudopotentials in the phonon calculations. $24 \times 24 \times 24$ ($30 \times 30 \times 32$) *k* grid and $4 \times 4 \times 4$ ($3 \times 3 \times 4$) *q* grid are used for α phase (γ phase) MoC in the DFPT calculations. The energy cutoff is 40 Ry (400 Ry) for wave-function (charge density) calculations. 0.02 Ry broadening is set in the Fermi-Dirac distribution for phonon mode calculations. The total electron-phonon coupling is given by

$$\lambda = \sum_{\mathbf{q}^v} \lambda_{\mathbf{q}^v}, \quad (1)$$

where λ_{qv} is the electron phonon coupling strength for different phonon state,

$$\lambda_{qv} \simeq \frac{1}{N_F \omega_{qv}} \sum_{mn, \mathbf{k}} |g_{mn}^v(\mathbf{k}, \mathbf{q})|^2 \delta(\varepsilon_{n\mathbf{k}}) \delta(\varepsilon_{m\mathbf{k}+\mathbf{q}}), \quad (2)$$

g_{mn}^v is the dynamical matrix and N_F is the density of states at the Fermi level for a single spin. ω_{qv} and $\varepsilon_{n\mathbf{k}}$ are the energy eigenvalues of phonon bands and electron bands, respectively. The transition temperature T_C is calculated by using the McMillan formula [57,58],

$$T_C \simeq \frac{\bar{\omega}_{\log}}{1.2} \exp \left[\frac{1.04(1 + \lambda)}{\mu^*(1 + 0.62\lambda) - \lambda} \right], \quad (3)$$

where μ^* is the Morel-Anderson pseudopotential [59] and is usually set between 0.1 and 0.2. It describes the effective electron-electron Coulomb repulsion. $\bar{\omega}_{\log}$ describes the

average of phonon frequency. To simulate the charge doping, we change the total number of electrons in one unit cell artificially and insert a uniform charge background to keep the system charge neutral. The self-consistent DFT and DFPT calculations are repeated for each doping concentration.

ACKNOWLEDGMENTS

H.T.J. is supported by the Ministry of Science and Technology, Taiwan, and thanks NCHC, CINC-NTU, and NCTS, Taiwan, for technical support. T.-R.C. is supported by the Ministry of Science and Technology under the MOST Grant for the Columbus Program No. 107-2636-M-006-004-, National Cheng Kung University, and National Center for Theoretical Sciences (NCTS), Taiwan. W.X. is thankful for support from the State of Louisiana, Board of Regents, under Contract No. LEQSF(2017-20)-RD-A-08 and Shared Instrumentation Facility at Louisiana State University for the SEM-EDS measurements.

-
- [1] J. Alicea, Y. Oreg, G. Refael, F. von Oppen, and M. P. A. Fisher, *Nat. Phys.* **7**, 412 (2011).
- [2] C. Nayak, S. H. Simon, A. Stern, M. Freedman, and S. D. Sarma, *Rev. Mod. Phys.* **80**, 1083 (2008).
- [3] L. Fu, *Phys. Rev. Lett.* **106**, 106802 (2011).
- [4] T. H. Hsieh, H. Lin, J. Liu, W. Duan, A. Bansil, and L. Fu, *Nat. Comm.* **3**, 982 (2012).
- [5] M. Legner, A. Rüegg, and M. Sigrist, *Phys. Rev. Lett.* **115**, 156405 (2015).
- [6] B.-J. Yang and N. Nagaosa, *Nat. Comm.* **5**, 4898 (2014).
- [7] L. Fu, C. L. Kane, and E. J. Mele, *Phys. Rev. Lett.* **98**, 106803 (2007).
- [8] C. L. Kane and E. J. Mele, *Phys. Rev. Lett.* **95**, 226801 (2005).
- [9] C.-K. Chiu, J. C. Y. Teo, A. P. Schnyder, and S. Ryu, *Rev. Mod. Phys.* **88**, 035005 (2016).
- [10] M. Z. Hasan and C. L. Kane, *Rev. Mod. Phys.* **82**, 3045 (2010).
- [11] L. Fu and C. L. Kane, *Phys. Rev. Lett.* **100**, 096407 (2008).
- [12] B. A. Bernevig and T. L. Hughes, *Topological Insulators and Topological Superconductors* (Princeton University Press, Princeton, NJ, 2013).
- [13] M. Sato and Y. Ando, *Rep. Prog. Phys.* **80**, 076501 (2017).
- [14] S.-Y. Xu, N. Alidoust, I. Belopolski, A. Richardella, C. Liu, M. Neupane, G. Bian, S.-H. Huang, R. Sankar, C. Fang, B. Dellabetta, W. Dai, Q. Li, M. J. Gilbert, F. Chou, N. Samarth, and M. Z. Hasan, *Nat. Phys.* **10**, 943 (2014).
- [15] Q. L. He, L. Pan, A. L. Stern, E. C. Burks, X. Che, G. Yin, J. Wang, B. Lian, Q. Zhou, E. S. Choi, K. Murata, X. Kou, Z. Chen, T. Nie, Q. Shao, Y. Fan, S.-C. Zhang, K. Liu, J. Xia, and K. L. Wang, *Science* **357**, 294 (2017).
- [16] T.-R. Chang, P.-J. Chen, G. Bian, S.-M. Huang, H. Zheng, T. Neupert, R. Sankar, S.-Y. Xu, I. Belopolski, G. Chang, B. Wang, F. Chou, A. Bansil, H.-T. Jeng, H. Lin, and M. Z. Hasan, *Phys. Rev. B* **93**, 245130 (2016).
- [17] S.-Y. Guan, P.-J. Chen, M.-W. Chu, R. Sankar, F. Chou, H.-T. Jeng, C.-S. Chang, and T.-M. Chuang, *Sci. Adv.* **2**, e1600894 (2016).
- [18] G. Bian, T.-R. Chang, A. Huang, Y. Li, H.-T. Jeng, D. J. Singh, R. J. Cava, and W. Xie, *Phys. Rev. Mater.* **1**, 021201(R) (2017).
- [19] M.-X. Wang, C. Liu, J.-P. Xu, F. Yang, L. Miao, M.-Y. Yao, C. L. Gao, C. Shen, X. Ma, X. Chen, Z.-A. Xu, Y. Liu, S.-C. Zhang, D. Qian, J.-F. Jia, and Q.-K. Xue, *Science* **336**, 52 (2012).
- [20] T. H. Hsieh and L. Fu, *Phys. Rev. Lett.* **108**, 107005 (2012).
- [21] P.-J. Chen, T.-R. Chang, and H.-T. Jeng, *Phys. Rev. B* **94**, 165148 (2016).
- [22] S. Mitra, K. Okawa, S. K. Sudheesh, T. Sasagawa, J.-X. Zhu, and E. E. M. Chia, *Phys. Rev. B* **95**, 134519 (2017).
- [23] M. Neupane, N. Alidoust, M. M. Hosen, J.-X. Zhu, K. Dimitri, S.-Y. Xu, N. Dhakal, R. Sankar, I. Belopolski, D. S. Sanchez, T. R. Chang, H.-T. Jeng, K. Miyamoto, T. Okuda, H. Lin, A. Bansil, D. Kaczorowski, F. Chou, M. Z. Hasan, and T. Durakiewicz, *Nat. Comm.* **7**, 13315 (2016).
- [24] H. Choi, M. Neupane, T. Sasagawa, E. E. M. Chia, and J.-X. Zhu, *Phys. Rev. Mater.* **1**, 034201 (2017).
- [25] R. H. Willens, E. Buehler, and B. T. Matthias, *Phys. Rev.* **159**, 327 (1967).
- [26] C. I. Sathish, Y. Shirako, Y. Tsujimoto, H. L. Feng, Y. Sun, M. Akaogi, and K. Yamaura, *Solid State Commun.* **177**, 33 (2014).
- [27] S.-H. Jhi, S. G. Louie, M. L. Cohen, and J. Ihm, *Phys. Rev. Lett.* **86**, 3348 (2001).
- [28] L. Bellaiche and D. Vanderbilt, *Phys. Rev. B* **61**, 7877 (2000).
- [29] J. Ren, G. Bian, L. Fu, C. Liu, T. Wang, G. Zha, W. Jie, M. Neupane, T. Miller, M. Z. Hasan, and T.-C. Chiang, *Phys. Rev. B* **90**, 205211 (2014).
- [30] E. V. Clougherty, K. H. Lothrop, and J. A. Kafalas, *Nature* **191**, 1194 (1961).
- [31] A. A. Burkov, M. D. Hook, and L. Balents, *Phys. Rev. B* **84**, 235126 (2011).
- [32] C. Fang, Y. Chen, H.-Y. Kee, and L. Fu, *Phys. Rev. B* **92**, 081201 (2015).
- [33] G. Bian, T.-R. Chang, R. Sankar, S.-Y. Xu, H. Zheng, T. Neupert, C.-K. Chiu, S.-M. Huang, G. Chang, I. Belopolski, D. S. Sanchez, M. Neupane, N. Alidoust, C. Liu, B. Wang, C.-C. Lee, H.-T. Jeng, C. Zhang, Z. Yuan, S. Jia, A. Bansil, F. Chou, H. Lin, and M. Z. Hasan, *Nat. Comm.* **7**, 10556 (2016).
- [34] G. Bian, T.-R. Chang, H. Zheng, S. Velury, S.-Y. Xu, T. Neupert, C.-K. Chiu, S.-M. Huang, D. S. Sanchez, I. Belopolski, N.

- Alidoust, P.-J. Chen, G. Chang, A. Bansil, H.-T. Jeng, H. Lin, and M. Z. Hasan, *Phys. Rev. B* **93**, 121113(R) (2016).
- [35] K. Kuo and G. Hägg, *Nature* **170**, 245 (1952).
- [36] G. Chang, S.-Y. Xu, S.-M. Huang, D. S. Sanchez, C.-H. Hsu, G. Bian, Z.-M. Yu, I. Belopolski, N. Alidoust, H. Zheng, T.-R. Chang, H.-T. Jeng, S. A. Yang, T. Neupert, H. Lin, and M. Z. Hasan, *Sci. Rep.* **7**, 1688 (2017).
- [37] J.-P. Sun, D. Zhang, and K. Chang, *Chin. Phys. Lett.* **34**, 027102 (2017).
- [38] L. Fu and C. L. Kane, *Phys. Rev. B* **76**, 045302 (2007).
- [39] R. Yu, X.-L. Qi, A. Bernevig, Z. Fang, and X. Dai, *Phys. Rev. B* **84**, 075119 (2011).
- [40] E. I. Isaev, S. I. Simak, and I. A. Abrikosov, R. Ahuja, Yu. Kh. Vekilov, M. I. Katsnelson, A. I. Lichtenstein, and B. Johansson, *J. Appl. Phys.* **101**, 123519 (2007).
- [41] G. L. W. Hart and B. M. Klein, *Phys. Rev. B* **61**, 3151 (2000).
- [42] E. I. Isaev, R. Ahuja, and S. I. Simak, A. I. Lichtenstein, Yu. Kh. Vekilov, B. Johansson, and I. A. Abrikosov, *Phys. Rev. B* **72**, 064515 (2005).
- [43] N. S. Athanasiou, *Mod. Phys. Lett. B* **11**, 939 (1997).
- [44] P. Szabó, T. Samuely, V. Hašková, J. Kačmarčík, M. Žemlička, M. Grajcar, J. G. Rodrigo, and P. Samuely, *Phys. Rev. B* **93**, 014505 (2016).
- [45] K. E. Wagner, E. Morosan, Y. S. Hor, J. Tao, Y. Zhu, T. Sanders, T. M. McQueen, H. W. Zandbergen, A. J. Williams, D. V. West, and R. J. Cava, *Phys. Rev. B* **78**, 104520 (2008).
- [46] G. W. Webb, F. Marsiglio, and J. E. Hirsch, *Phys. C* **514**, 17 (2015).
- [47] W. Meissner and H. Franz, *Z. Physik* **65**, 30 (1930).
- [48] G. Kresse and J. Hafner, *Phys. Rev. B* **48**, 13115 (1993).
- [49] G. Kresse and J. Furthmüller, *Comput. Mater. Sci.* **6**, 15 (1996).
- [50] G. Kresse and J. Furthmüller, *Phys. Rev. B* **54**, 11169 (1996).
- [51] J. P. Perdew, K. Burke, and M. Ernzerhof, *Phys. Rev. Lett.* **77**, 3865 (1996).
- [52] G. Kresse and D. Joubert, *Phys. Rev. B* **59**, 1758 (1999).
- [53] P. E. Blöchl, *Phys. Rev. B* **50**, 17953 (1994).
- [54] C. Franchini, R. Kovik, M. Marsman, S. S. Murthy, J. He, C. Ederer, and G. Kresse, *J. Phys.: Condens. Matter* **24**, 235602 (2012).
- [55] H. J. Zhang, C. X. Liu, X. L. Qi, X. Dai, Z. Fang, and S. C. Zhang, *Nat. Phys.* **5**, 438 (2009).
- [56] A. A. Soluyanov and D. Vanderbilt, *Phys. Rev. B* **83**, 035108 (2011).
- [57] W. L. McMillan, *Phys. Rev.* **167**, 331 (1968).
- [58] P. B. Allen and R. C. Dynes, *Phys. Rev. B* **12**, 905 (1975).
- [59] P. Morel and P. W. Anderson, *Phys. Rev.* **125**, 1263 (1962).